Bio-Design and Manufacturing
https://doi.org/10.1631/bdm.2300253

RESEARCH ARTICLE

Magnesium and gallium coloaded microspheres accelerate bone repair via osteogenesis and antibiosis

Jin Bai[1,2] · Si Shen[1,2] · Yan Liu[1] · Shendan Xu[2] · Tianqi Li[1,2] · Zirou Wang[1] · Weili Liu[1] · Lingling Pu[1] · Gang Chen[2] · Xinxing Wang[1]

Received: 20 September 2023 / Accepted: 15 September 2024

Abstract

Bone defects have serious economic and clinical impacts; however, despite improvements in bone defect management, the range of clinical outcomes remains limited. A variety of biomaterials have been used to treat complex bone defects. However, final bone repair outcomes may be adversely affected by poor osteogenic capacity and risk of infection. Consequently, therapeutic methods are required that reduce bacterial contamination and increase the use of osteogenic biomaterials. Herein, we report the preparation of poly (lactic acid-coglycolic acid) (PLGA) microspheres coloaded with magnesium (Mg^{2+}) and gallium (Ga^{3+}) ions (Mg-Ga@PLGA), which can fill irregular bone defects and show good biosafety. During in vitro testing, Mg-Ga@PLGA not only showed a synergistic effect on promoting osteogenic differentiation but also inhibited osteoclastic differentiation. Moreover, we also found that Mg-Ga@PLGA demonstrated a strong antibacterial effect. In vivo, Mg-Ga@PLGA exhibited strong in situ osteogenic ability. In conclusion, Mg-Ga@PLGA has good potential for treating bone defects at risk of infection.

Graphic abstract

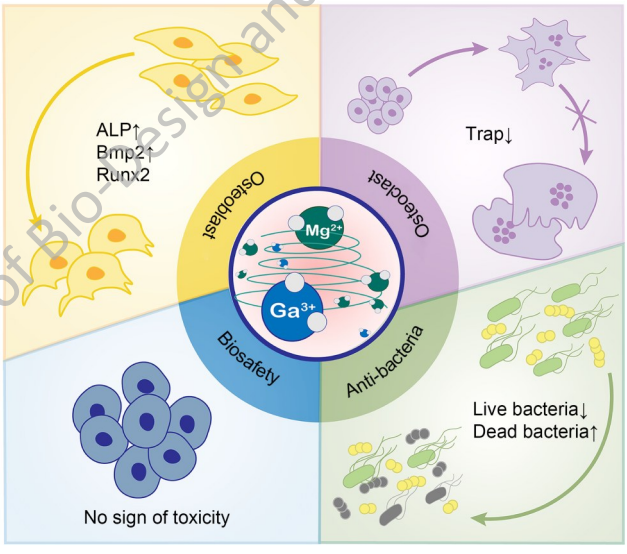

Keywords Microsphere · Osteogenesis · Antibacteria · Magnesium · Gallium

✉ Gang Chen
doctorchen@tmu.edu.cn

✉ Xinxing Wang
wxxemail@sina.cn

[1] Tianjin Institute of Environmental and Operational Medicine, Tianjin 300050, China

[2] School and Hospital of Stomatology, Tianjin Medical University, Tianjin 300070, China

1 Introduction

Bone defects caused by infection, tumor resection, and mechanical trauma [1] are major contributors cause functional failure and consequently contribute to reduced quality of life. Although bone grafting [2, 3] is used to treat bone defects, this solution has technical problems [4], including restricted sources, potential risk of infection, and immune rejection [5]. Bone grafting also poses socioeconomic challenges, including high cost, the necessity of multiple invasive surgeries, and a general lack of donors [6].

To facilitate proper bone regeneration, a bionic bone material based on cells should recruit stem or progenitor cells to the site of tissue injury via a biological scaffold then provide an osteo-friendly microenvironment for recruited cells [3, 7]. This allows colonization *in situ*, where the differentiation of stem and/or progenitor cells into a specific cell lineage is effectively promoted [8]. It is also important for such a scaffold to be biocompatible and result in no significant host tissue inflammation [9]. Recently, bioresorbable microspheres have received increased research interest as multiple drug delivery vectors [10–12]. In addition, microspheres containing bioactive components create a microenvironment that is suitable for cell differentiation [13]. Furthermore, microspheres can be used as an injectable material for tissue therapy and as a freeze-dried powder for filling irregularly-shaped bone defects [14, 15].

In this study, we designed an efficient protocol to generate poly (lactic acid-coglycolic acid) (PLGA) microspheres encapsulating magnesium and gallium ions (Mg-Ga@PLGA). The incorporation of Mg^{2+} into bone mineral (i.e., hydroxyapatite, HA) lattices has been found to markedly affect natural bone mineral density and biomechanics [16, 17]. Molecular level studies have found that Mg^{2+} may promote osteogenic gene expression via the RAS/RAF/MEK/ERK and Bmp2/Runx2 signaling pathways [18–20]. However, the use of Mg^{2+} alone as a bioactive ingredient can only lead to osteogenic differentiation-promoting effects, making it important to find effective bioactive combinations [21, 22].

To date, gallium (Ga) has been widely used in communications technologies, energy, computers, and space exploration [23]. Ga-containing biomaterials offer new options for the repair of osteoporotic bone defects by conferring the ability to inhibit the osteoclastic effect. Moreover, it can also improve repair outcomes while avoiding liver and kidney damage [24, 25]. In addition to the negative effect on osteoclastic cells, Gallium nitrate (GN) can also exert antibacterial activity against methicillin-resistant *Staphylococcus aureus* [26], *Escherichia coli*, and *Pseudomonas aeruginosa* [27–29]. Ga can be used as a direct wound-filling antimicrobial agent to prevent surgical failure caused by bacterial infection during the placement of biological scaffolds in the body [30, 31]. Based on Mg^{2+} induced osteogenesis and the antibacterial effects of Ga^{3+}, we therefore hypothesized that Ga^{3+} and Mg^{2+} codoped into PLGA microspheres could enhance bone defect repair.

2 Materials and Methods

2.1 Materials

Dichloromethane (DCM, HPLC grade, ⩾99.9%, MW: 84.93 Da), poly (vinyl alcohol) (PVA, viscosity: 3.5–4.5 mPaS, Alcoholysis degree: 97.5–99%, MW: 44.05 Da), $Ga(NO_4)_3$, $MgSO_4$, and PLGA (50:50, Mw: 38,000–54, 000) were obtained from Aladdin (Shanghai, China).

2.2 Microsphere synthesis

A modified water-in-oil-in-water (W1/O/W2) emulsion method was used to prepare Mg@PLGA microspheres. Briefly, PLGA (100 mg) was added slowly and dropwise into 4 mL of DCM; this mixture is hereafter referred to as "O." Next, 20 (wt%) $MgSO_4$ and 2% $Ga(NO_4)_3$ powders were dispersed into 1% (wt%) PVA to form a solution referred to here as "W2." We then added 1 mL of ultrapure water, which was the internal aqueous phase (W1), drop by drop to the oil phase in a blender. This was then stirred to obtain a W1/O mixture. The resulting W1/O solution was quickly poured into a 100 mL aliquot of W2, and this mixture was then stirred to obtain a compound emulsion. Stirring continued for 24 h until the DCM had completely evaporated. Next, the resulting suspension was centrifuged at 3000 rpm, the supernatant was discarded, and the pellet was cleaned before being centrifuged again (3, 000 rpm) to collect the microspheres, which were then freeze dried.

2.3 Morphological characterization.

A scanning electron microscope (HITACHI SU8100, Tokyo, Japan) was used to characterize the morphology of microspheres. Moreover, the mean radius was obtained by using multiple morphologies to count and quantify spheres. All tests used ImageJ software for image analysis (NIH, Bethesda, MD, USA).

2.4 Elemental analysis

Elemental mapping was carried out using a scanning electron microscope (HITACHI SU8100). Moreover, the metallic elements encased within the spheres were further quantified using X-ray photoelectron spectroscopy (XPS) (ESCALAB 250XI, Thermo Fisher Scientific, Waltham, MA, USA).

2.5 Mg^{2+} and Ga^{3+} release kinetics

To assess the release kinetics of Mg^{2+} and Ga^{3+}, we immersed 30 mg of Mg-Ga@PLGA in 10 mL of phosphate-buffered saline (PBS). This mixture was then incubated at 37 °C on a magnetic mixer and mixed thoroughly (60 rpm). Subsequently, 2 mL of the supernatant was removed at 7, 10, 20, 30, and 60 d, respectively. The Mg and Ga concentrations of this supernatant were then measured using Inductively Coupled Plasma Optical Emission spectroscopy (ICP-OES) (Agilent 7800, Santa Clara, CA, USA) while supplementing with equal amounts of PBS.

2.6 Cytotoxicity and cell adhesion analyses

Next, we labeled live and dead cells with Calcein-AM/propidium iodide (PI) double staining to detect cell death after 3 days of coculturing (YEASEN, Shanghai, China). We also used mouse embryo osteoblast precursor cells (MC3T3-E1s) and bone marrow-derived macrophages (BMMs) to observe the cytoskeleton. MC3T3-E1s were fixed in 4% paraformaldehyde after 3 days of culturing and BMMs were fixed at the 3rd day after inoculation with 5mg microspheres in 1mL medium. These solutions were then washed with PBS, stained with 50 μg/mL Cy3-ghost cyclopeptide for 40 min, then visualized using confocal laser scanning microscopy (CLSM; Carl Zeiss, Oberkochen, Germany). This was performed to determine the number of cells at the early stage of adhesion and to characterize their cell morphology, pseudopod extension, and cytoskeletal aggregation.

The vertical migration of cells was assessed using transwell assays. To assess the effect of the slow release of Mg^{2+} and Ga^{3+} from microspheres on the migration of MC3T3-E1s, we placed 5 mg microspheres in 1 mL medium in the lower transwell chamber then placed cells in the upper chamber. After 48 h, the cells above the porous membrane were mechanically removed and the cells on the lower surface of the membrane were fixed using 4% (*v*/*v*) paraformaldehyde and stained via incubation with hematoxylin (Solarbio) solution for 10 min. Images were then taken under a light microscope and the cells were quantified using image analysis with ImageJ.

2.7 Evaluation of apoptosis and cell proliferation

Next, MC3T3-E1s or BMMs were inoculated and cocultured with 5 mg microspheres in 1 mL medium. On day 3, the cells were centrifuged and the supernatant was removed. These cells were then stained using BD Annexin V (BD Pharmingen, San Jose, CA, USA) by gently resuspending the cells in a BD Annexin V solution and incubating them for 20 min at 37 °C in the dark. Cells were then analyzed using flow cytometry with a BD LSRFortessa instrument (BD Biosciences, San Jose, CA, USA). FlowJo software (TreeStar, Ashland OR, USA) was then used to analyze these data.

Next, we assessed cell proliferation using a Cell Counting Kit-8 (CCK-8; Biosharp). Briefly, 5×10^3 MC3T3-E1s or 1×10^5 BMMs were inoculated into 96-well plates and 5 mg microspheres in 1 mL medium were added and cocultured with the after 24 hours of cell apposition. The CCK-8 assay solution was added at various times according to the manufacturer's instructions. Optical density values were recorded at 450 nm using an enzyme marker (Spectra Max, Molecular Devices, Berlin, Germany).

2.8 Assessment of osteogenesis effect and osteoclast differentiation in vitro

Next, alkaline phosphatase (ALP) activity was determined using a 5-bromo-4-chloro-3-indolyl phosphate (BCIP)/nitro blue tetrazolium Chromogen Kit (Solarbio). As per the kit's instructions, the provided solutions were mixed and added to each plate to facilitate staining of the cells for 8 h in the dark. Thereafter, the cells were observed using a light microscope then quantified using ImageJ.

Twenty-one days after the start of culturing, cells were washed with PBS three times, then fixed using 95% (*v*/*v*) ethanol with Alizarin Red S (ARS) Stain Solution (Beyotime, Jiangsu, China). These cells were photographed under an inverted microscope and quantified using ImageJ.

Subsequently, osteogenic markers were detected using immunofluorescence after 5 days of cell culturing. ß-tubulin was chosen as a morphological marker, and Bmp2 and Runx2 were used as osteogenic markers. Cells were incubated with primary antibodies recognizing these proteins (1:200, Abcam, Cambridge, UK) overnight at 4 °C as well as secondary antibodies comprising goat anti-rabbit IgG conjugated with corallite 594 or corallite 488 (1:200, ProteinTech, Wuhan, China). Nuclei were labeled using DAPI and CLSM was used to obtain fluorescence images. The levels of osteogenic proteins were estimated using Western blotting, then total protein samples were extracted and quantified. Following a standard protocol, we incubated total protein samples with primary antibodies recognizing Bmp2, ALP, and Runx2 (1:1000, Affinity Biosciences, Jiangsu, China) and appropriate secondary antibodies (1:1000, ProteinTech) for 1 h at room temperature. Protein levels were reported relative to GAPDH (1:10, 000, Abcam), which was used as an internal control. Visualization of immunoreactive proteins was then performed using BeyoECL Plus (Beyotime), and their levels were then quantified using ImageJ.

For TRAP staining, BMMs were first seeded at 1×10^5 per well in 24-well plates. The specific differentiation protocol used here was described above. On the 5th day of differentiation, cells were fixed in paraformaldehyde for

10 min, rinsed three times using PBS, then stained using a tartrate-resistant acid phosphatase (TRAP) staining kit (Sigma, St. Louis, MO, USA) with all procedures performed according to the manufacturers' protocol.

2.9 Analysis of antibacterial effect in vitro

Next, we used *S. aureus* (gram-positive) and *E. coli* (gram-negative) to test the antibacterial activity of the Mg@PLGA microspheres. Next, the concentrations of the two types of bacteria were adjusted to a density of 1×10^6 colony forming units (CFU)/mL in a broth medium. Subsequently, 50 mg of sterilized microspheres were immersed in 5 mL sterile deionized water to prepare extracts. After 6 hours of shaking at 37 °C, we removed 100 μL aliquots of the bacterial solution and plated them onto brain heart infusion (BHI) agar plates. These were then incubated for 24 h after which the CFU was determined.

We then performed an inhibitory zone experiment. To do so, 100 μL of a solution containing bacteria at a concentration of 1×10^9 CFU/mL was spread on BHI agar plates and these plates were then incubated for 30 minutes at 37 °C with 10 mg of sterilized microspheres immersed in 1 mL sterile deionized water. After colonization, holes were made in the agar plates to which we added 30 μL of sample extracts. A hole containing PLGA served as an experimental control. After 24 h of culturing at 37 °C, the inhibitory zone was measured.

Live/dead staining revealed the extent of the microspheres' antibacterial effect. We examined 100 mg samples of four types of microspheres; each sample was placed in 10 mL of a solution containing 1×10^6 CFU/mL of bacteria and the resulting culture was incubated at 37 °C after being diluted 100 times in medium. In addition, after 24 h of growth, bacteria were stained using a live/dead staining kit, and fluorescence images were acquired using CLSM.

2.10 Assessment of in vivo bone regeneration

All animal experiments followed the protocol for the care and use of the experimental animals approved by the Institutional Animal Care and Use Committee of Yi Shengyuan Gene Technology (Tianjin) Company (Approval No. YSY-DWLL-2022108). In brief, male Wistar rats (6–8 weeks old) were selected to establish a critical cranial defect model (8 mm) and were divided into five groups, including one blank (untreated) control group, and four groups with defects treated using 20 mg microspheres. Animal models were established according to a standard protocol. In brief, under aseptic conditions a defect of 8 mm in diameter was made in the median line of the skull using a ring drill. Microspheres were then implanted into the defects, and the defect was then covered with a barrier membrane and the skin was sutured and sterilized. During the procedure we ensured that the rat subject's airway was open to prevent asphyxia. All rats were free to move around, eat, and drink.

Twelve weeks after surgery, rats were sacrificed, and their skulls were obtained and fixed using 4% paraformaldehyde. Micro-CT (Perkin-Elmer, Waltham, MA, USA) was then used to scan and reconstruct images of fixed skulls. CTvox software (Bruker, Billerica, MA, USA) was used to view images and CTAn software (Bruker) was used to perform analyses of images obtained. Fixed cranial samples were subjected to decalcification and dehydration, before being embedded and cut into sections 5 μm thick. These sections were then subjected to hematoxylin and eosin (H&E) staining, Masson staining, and immunohistochemistry (IHC) staining using anti-Bmp2, COL I, OCN, and OPN antibodies (1:200, Abcam, UK). IHC samples were then incubated with the appropriate secondary antibodies before all stained sampled were imaged under an inverted microscope (Olympus, Tokyo, Japan).

Finally, to assess MP biosafety in vivo, blood IL-6 and TNF-α levels were measured using commercially available ELISA kits (Kexing, Jinan, China) to assess the level of systemic inflammation.

2.11 Evaluation of the antibacterial effect in vivo

Using the bone defect model described above, we placed a *S. aureus* bacterial solution (10^7 CFU in 100 μL of sterile saline) on the defect before wound closing to create an infection [32]. This solution contained bacteria that were either mixed with or without 20 mg microspheres; after solution addition the wound was closed with sutures. After 3 days, the cranial bone was re-exposed to collect granulation tissue (1 mm^3). Obtained granulation tissue was transferred to 10 mL of sterile saline, then 100 μL of this liquid was transferred and spread to an agar plate. Agar plates were incubated at 37 °C for 24 h before CFU determination. In addition, we also obtained extracts of granulation tissue (1 mm^3) and assessed infection by performing qRT-PCR for TNF-α and IL-6. The primers for all genes tested by qRT-PCR are shown in Table S1.

2.12 Statistical analysis

The mean ± standard deviation was used to summarize quantitative data measurements. One-way analysis of variance and t-tests were used to determine the statistical significance of differences in means. $p<0.05$ was considered to be the threshold of statistically significant differences; $p<0.01$ indicated a very significant difference.

3 Results and Discussion

3.1 Characteristics of Mg-Ga@PLGA microspheres

Figure 1a shows the SEM characterization of the microsphere morphology. The Mg-Ga@PLGA microspheres had rough surfaces because of the deposition of inorganic salts. Fig. 1b shows qualitative results of the elemental mapping of Mg-Ga@PLGA microspheres. A good scaffold must be loaded with key factors, and provide space for cells to recruit and grow stem cells in vivo [33]. In addition to cell growth, the microsphere scaffold must have a gap for the initial capillaries to grow. This is because the growth of tiny blood vessels and capillaries is required to transport oxygen and nutrients to deeper tissues [34], thereby ensuring that high-quality new bone is produced. Here, the diameter of prepared microspheres was around 50μm (Fig. 1c). The microspheres were allowed to fill in any irregular defects to facilitate cell adhesion and provide support for new bone tissue [35].

Next, XPS was used to further analyze the distribution of Mg^{2+} and Ga^{3+} in the PLGA microspheres. Fig. 1d shows the loading content of Mg^{2+} and Ga^{3+}. From the enlarged spectra, we found that Ga^{3+} and Mg^{2+} were both loaded onto the PLGA microspheres. The atom percent of Mg—which was used to represent the loading efficiency in the PLGA microspheres—was 6.99%, which was 16 times higher than that of Ga.

The microsphere release patterns of Mg^{2+} and Ga^{3+} are shown in Fig. S1. After 10 days, the release rate reached a plateau. However, it did not reach 100%. This may be related to the nonspecific adsorption of ions on the microspheres and attrition resulting from preparation conditions. In general, this system guarantees a slow release of ions and maintains the local concentration of bioactive components, thereby facilitating the biological functions of Mg^{2+} and Ga^{3+}.

3.2 Biocompatibility

To test the biocompatibility of the Mg^{2+} and Ga^{3+} loaded PLGA microspheres, we created direct and indirect cultures of MC3T3-E1s and BMMs with the microspheres. Our data showed that none of the groups of microspheres inhibited the proliferation of MC3T3-E1s and BMMs relative to a blank control. Moreover, tests using Calcein-AM/PI probes allowed us to detect a few dead cells (Fig. 2a), suggesting that the microspheres were not cytotoxic.

Cytoskeleton staining further indicated that the cells were intact, showing a fully expanded polygonal shape, which was consistent with the observed fibroblast-like morphology of MC3T3-E1s [36]. In previous studies, confocal imaging has shown that fibroblasts adhered to the microspheres show a star-like phenotype [37]. MC3T3-E1s cocultured with microspheres had well-stretched bundles of actin (shown in red) with clear lines comprising actin filaments. Also visible were extended pseudopods, which indicated that the PLGA microspheres acted as a scaffold for cell extension and cytoskeleton development [38]. Finally, our results showed that the BMM had an intact morphology, with a rounded cytoskeleton near the nucleus and no obvious expansion. This is indicative of the primitive state of inactive macrophages (Fig. 2b).

Next, transwell assays were used to examine the migration and recruitment abilities of MC3T3-E1s. After 48 h of incubation, the coloaded Mg^{2+} and Ga^{3+} group showed higher numbers of migrating cells compared to PLGA and blank groups (Fig. 2c). Further quantitative analysis (Fig. S2) showed that the number of migrating cells significantly differed between the Mg-Ga@PLGA and blank groups ($p<0.0001$). In general, cytokines produced by trauma and the initial inflammatory process show poor stem cell recruitment ability [39, 40]. Here, the Mg^{2+} and Ga^{3+} groups showed marked promotion of MC3T3-E1s migration in vitro and a more prominent promigration effect after coloading [41].

As shown in Fig. 3, the results of the CCK-8 and flow cytometry assays showed that cells incubated with the four types of microspheres and control cells were highly similar. These results indicated that while the microspheres did not enhance cell proliferation, they also did not show obvious cytotoxicity. Moreover, MC3T3-E1s and BMMs from each group showed logarithmic proliferation. We found no statistically significant differences in the proportions of apoptotic cells were noted between the control and experimental groups, suggesting that the microspheres had no toxic effects on MC3T3-E1s and BMMs. In all groups tested, we found few early apoptotic cells (Q2) and late apoptotic cells (Q3). This demonstrated the high biosafety of PLGA microspheres and ensured that they were compatible with healthy cell proliferation and survival, a fact that was required for later study of the effect of microspheres on cell differentiation.

3.3 Mg-Ga@PLGAs increased osteoblast differentiation and inhibited osteoclast differentiation

Seven days after differentiation induction, Western blotting was performed to quantify the levels of osteogenesis-related proteins (Fig. 4a). Mg-Ga@PLGA showed highly significant increases in the levels of proteins related to osteogenic differentiation (Fig. 4b), demonstrating that coloading of these two elements resulted in a superior osteogenic differentiation effect relative to either Mg^{2+} or Ga^{3+} alone. By day 14 after the induction of differentiation, we were still able to observe an increase in the expression of osteogenesis-related

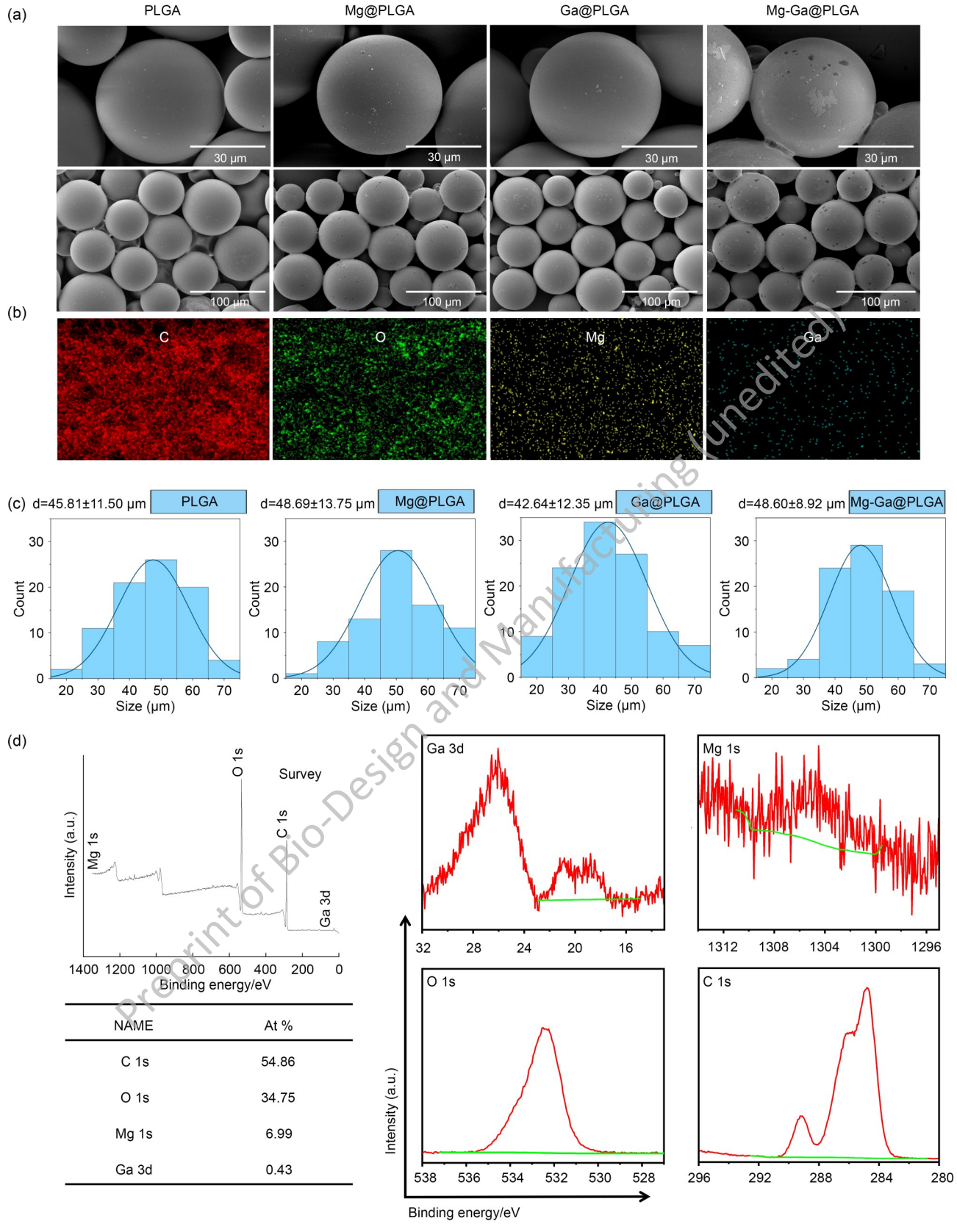

Fig. 1 Characteristics of the Mg-Ga@PLGA microspheres. (a) Under SEM observation, the microspheres showed a smooth surface and microstructure. (b) Elemental mapping of the microspheres. (c) Particle analysis size of the microspheres. (d) XPS spectra of the Mg-Ga@PLGA microspheres with enlarged spectra

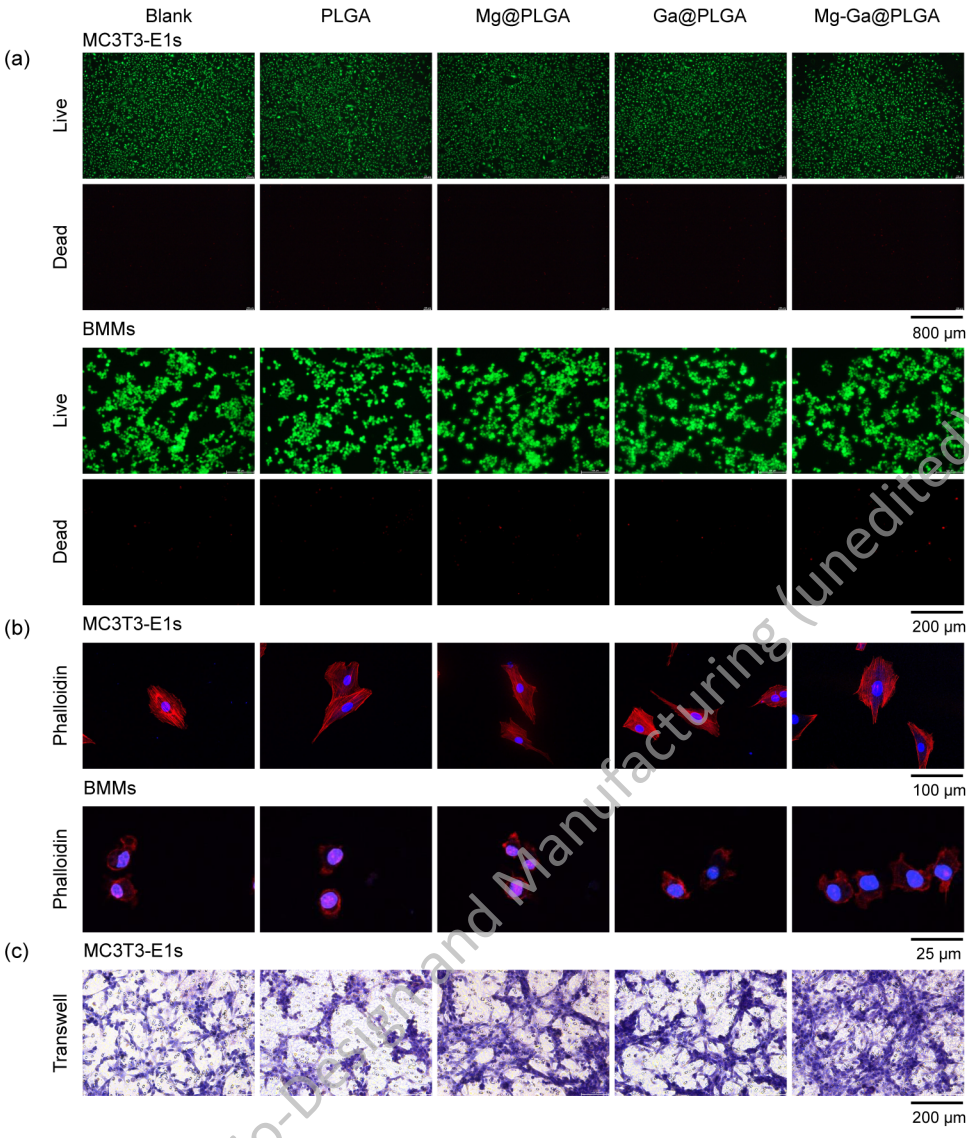

Fig. 2 Mg-Ga@PLGA microsphere biocompatibility. (a) Staining of live (Calcein-AM, green) and dead (PI, red) cells when cultured with various microspheres. (b) Staining of the cytoskeleton at 3 days post-seeding in each sample. (c) Effect of microsphere treatment on the migration of MC3T3-E1cells

proteins, except for ALP; these results were similar to the results observed on day 7. We speculate that it may be that, since ALP is an early osteogenic differentiation protein, ALP expression peaks at day 10 [42, 43] and then gradually decreases, leading to a point where there is no significant difference in its levels among groups. Next, we used immunofluorescence techniques to directly observe the location of typical osteogenesis-related proteins. By day 5 after osteogenic differentiation, Runx2 (shown in red) was found to distributed throughout the cytoplasm and nucleus, with the Mg-Ga@PLGA group showing increased levels of Runx2 in the nucleus. These observations indicate that Mg^{2+} and Ga^{3+} may synergistically promote Runx2 function in the nucleus [44] (Fig. 4c). In addition, Bmp2 showed aggregation in the cytoplasm. The Mg-Ga@PLGA group showed the strongest fluorescence intensity of osteogenic differentiation-related proteins (Fig. 4d), a finding that was consistent with our Western blotting results. Compared to other groups, the coloaded group showed a larger contribution to osteogenic differentiation (Fig. 4e), suggesting a possible synergistic effect of Mg^{2+} and Ga^{3+} during the osteogenic differentiation process.

To further validate these results, ALP staining and ARS staining were used to infer that osteogenic differentiation occurred in the presence of Mg-Ga@PLGA. Our findings clearly showed that the Mg-Ga@PLGA group showed the most obvious ALP and ARS staining signals, indicating that this group showed higher levels of ALP expression and more calcium deposition (Figs. 5a–5c and 5e–5g).

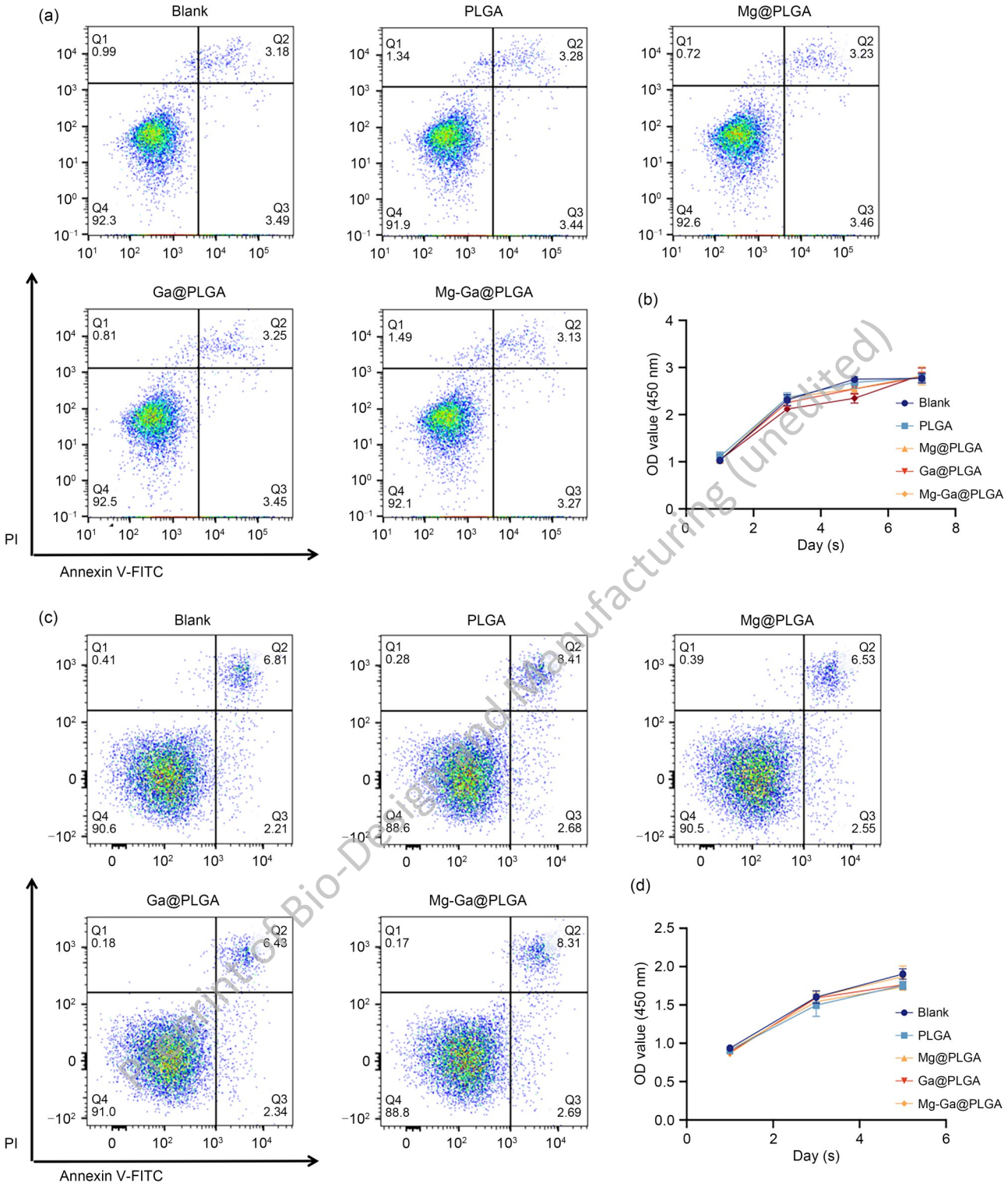

Fig. 3 Apoptosis caused by Mg-Ga@PLGA in vitro. (a, c) Flow cytometry analysis of Annexin-V staining of MC3T3-E1s and BMMs on day 3 of microsphere treatment. (b, d) According to CCK-8 assays, treatment with Mg-Ga@PLGA microsphere extracts caused no cytotoxicity toward MC3T3-E1s or BMMs

Taken together, these results show that the Mg-Ga@PLGA microspheres not only showed a superior osteogenic effect, but also showed an inhibitory effect with respect to osteoclastic differentiation. TRAP staining (Fig. 5d, h) showed that Ga^{3+} had a significant inhibitory effect on BMMs differentiation, and the presence of Mg^{2+} was

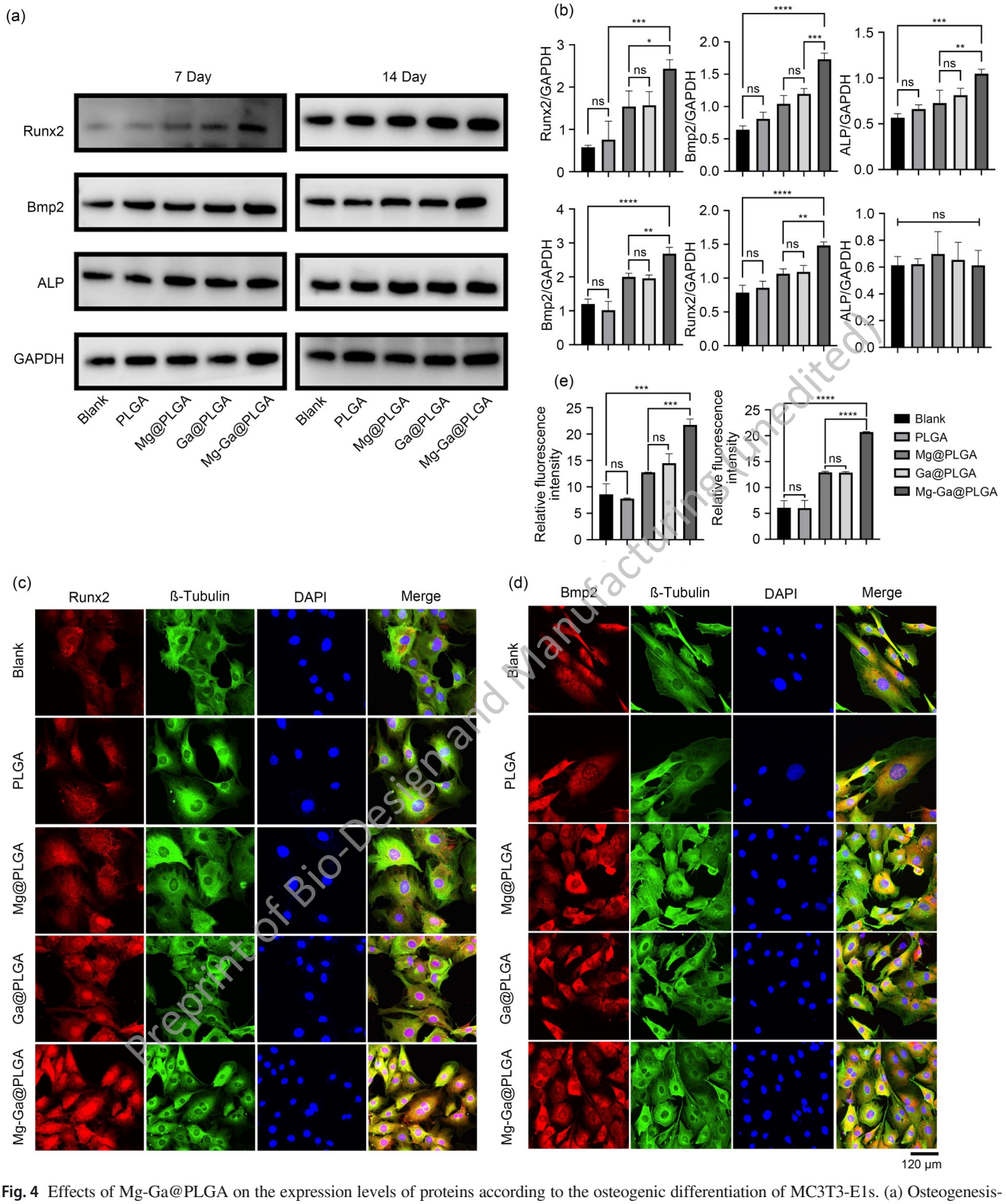

Fig. 4 Effects of Mg-Ga@PLGA on the expression levels of proteins according to the osteogenic differentiation of MC3T3-E1s. (a) Osteogenesis-related protein levels after 7 and 14 days of microsphere treatment. (b) Quantitative data derived from the western blotting results. (c) Images of immunofluorescence for Runx2 and (d) Bmp2, and (e) fluorescence intensity quantification after MC3T3-E1s were cultured with microspheres for 5 days. $^{***}p<0.001$, $^{****}p<0.0001$

found to enhance the inhibitory effect of Ga^{3+} on osteoclastic differentiation [31]. By the 5th day after the induction of osteoclastic differentiation, BMMs cultured with Mg-Ga@PLGA microspheres were still undifferentiated;

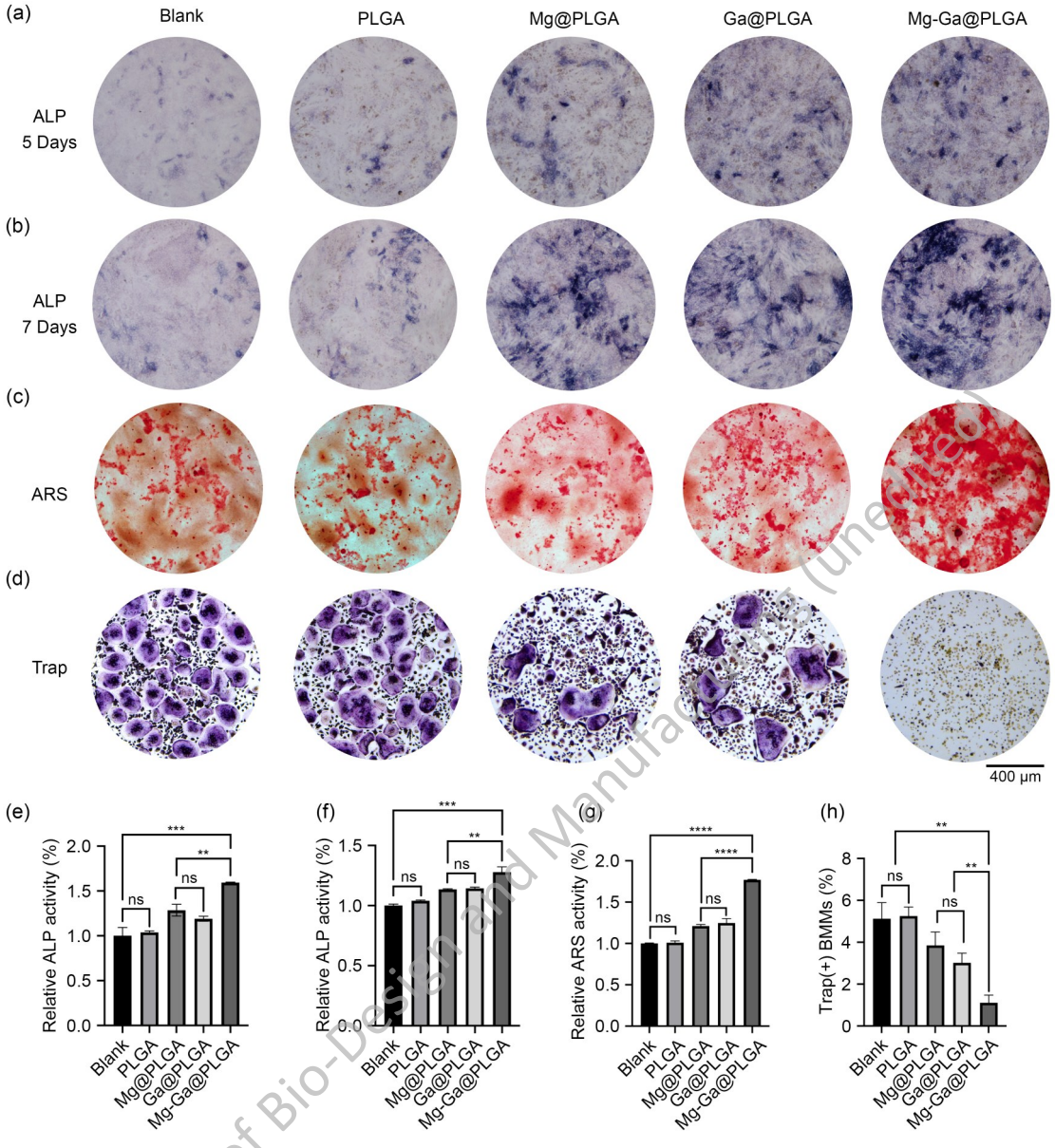

Fig. 5 Mg-Ga@PLGA's effects on MC3T3-E1 cell osteogenic differentiation. (a, b) Representative images of MC3T3-E1s treated with microspheres for 5 days and 7 days and then stained for ALP. (e, f) the quantification of relative ALP activities. (c) Images of ARS staining of MC3T3-E1s treated with microspheres for 21 days. (g) The quantification of ARS staining. (d) TRAP staining images of BMMs cultured with microspheres for 5 days and (h) quantification of TRAP-positive polynucleated (≥five nuclei) osteoclasts derived from BMMs. $^{*}p<0.05$, $^{**}p<0.01$, $^{***}p<0.001$, $^{****}p<0.0001$

this result indicated that Mg-Ga@PLGA inhibits the formation of osteoclasts.

3.4 The in vitro antibacterial activity of Mg-Ga@PLGA microspheres

Next, we used live/dead staining, total antibacterial activity tests, and the inhibition zone tests to evaluate the antibacterial properties of the microspheres (Fig. 6). We found few inhibition zones in the blank and Mg@PLGA groups; however, the inhibition zones of the Ga@PLGA and Mg-Ga@PLGA groups were significant for *S. aureus* and *E. coli* (Fig. 6a). Overall, the inhibition zone test showed that the Mg-Ga@PLGA microspheres exhibited the most significant antibacterial effect.

Subsequently, treatment with Ga@PLGA and Mg-Ga@PLGA resulted in significantly reduced numbers of bacterial colonies compared with blank and Mg@PLGA groups; Ga@PLGA and Mg-Ga@PLGA groups showed only sporadic bacterial colonization (Fig. 6b). Further live/dead staining tests (Fig. 6c) showed that almost all bacteria survived in the PLGA and Mg@PLGA groups (green),

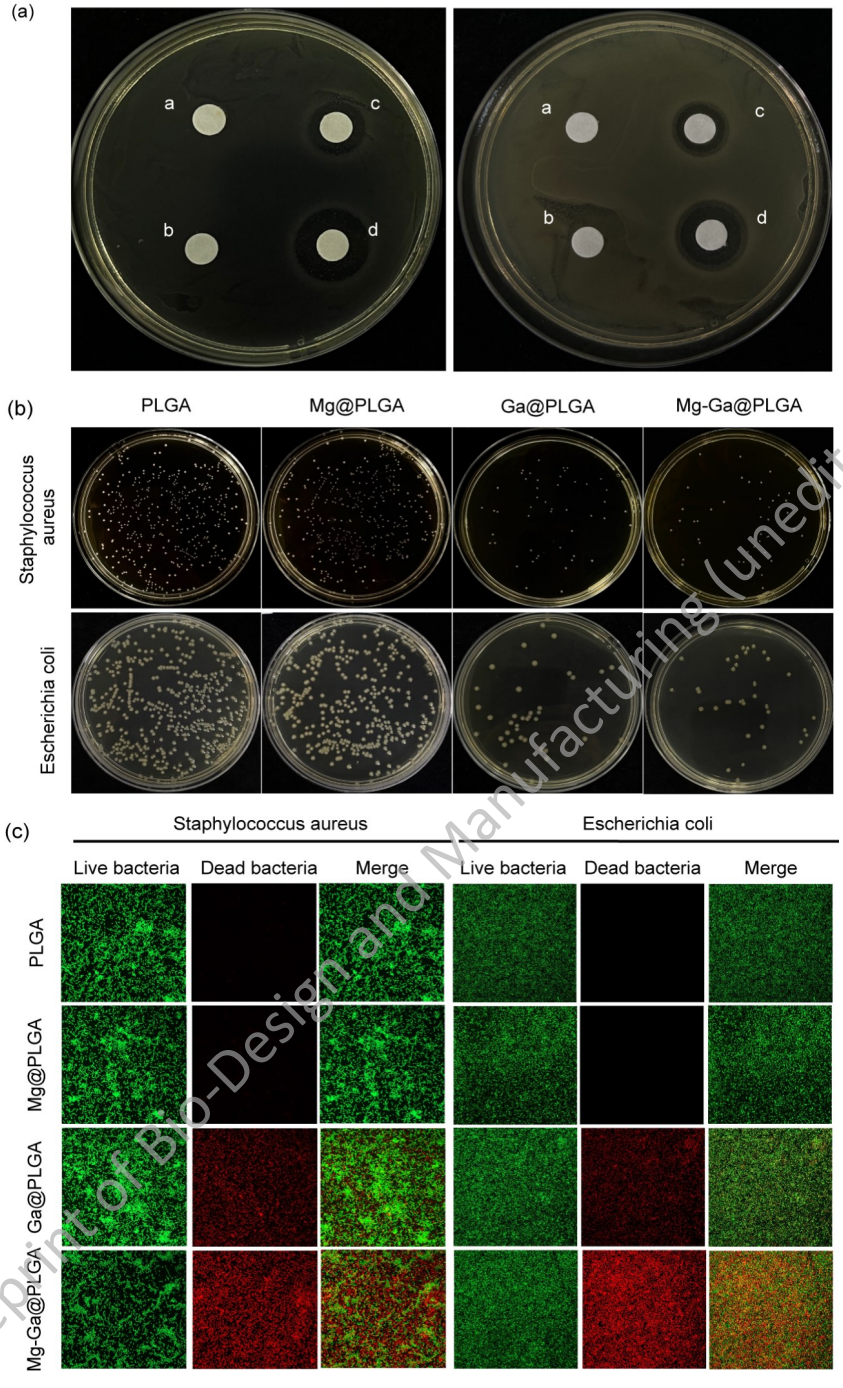

Fig. 6 Evaluation of the antibacterial properties of the microspheres. (a) *E. coli* and *S. aureus* inhibition zones when co-cultured for 24 h with microsphere extracts. [(a) blank, (b) Mg@PLGA (c) Ga@PLGA, and (d) Mg-Ga@PLGA]. (b) Total antibacterial activity (c) Live/dead staining of *E. coli* and *S. aureus*

whereas the Ga@PLGA and Mg-Ga@PLGA groups had far more dead bacteria. The relevant statistical results are shown in Fig. S3. Taken together these experiments demonstrated that Ga^{3+} showed a strong antibacterial effect and Mg^{2+} combined with Ga^{3+} retained this potent antibacterial activity. Furthermore, the antibiotic property of Ga^{3+} might be used to prevent bacteria from damaging bone healing and reduce risk of infection following bone damage.

It has been reported that the antimicrobial effect of Ga^{3+} may be related to the fact that it has a similar ionic radius as iron ions (Fe^{3+}) [45]. Importantly, many microbial uptake systems are unable to distinguish between Ga^{3+} and Fe^{3+} due to the similarity of their ion radii [29]. Therefore, bacterial infections may be inhibited by exploiting their nutrient

vulnerability [46]; for example, Ga^{3+} could compete with Fe^{3+} to disrupt Fe^{3+} metabolism. [47]. The antibacterial effect observed here may be able to reduce ameliorate inflammatory responses and induce osteogenic microenvironments to enhance osteogenesis itself [48].

Further in vitro assays showed that Mg-Ga@PLGA microspheres exerted a significant inhibition effect on bacteria. However, this effect was less consistent, which may be related to the fact that bacteria can absorb magnesium ions without limitation, and the fact that bacteria have various mechanisms to adapt to stress [49].

3.5 Mg-Ga@PLGA facilitated bone repair in rat skull defect models

The ability of Mg-Ga@PLGA to promote the repair of bone defects was evaluated using an 8 mm rat skull defect model. Micro-CT images of samples collected 12 weeks after surgery for each group showed the formation of new bone that progressed from the edge toward the center of the defect (Fig. 7a). Of the five groups studied, the Mg-Ga@PLGA

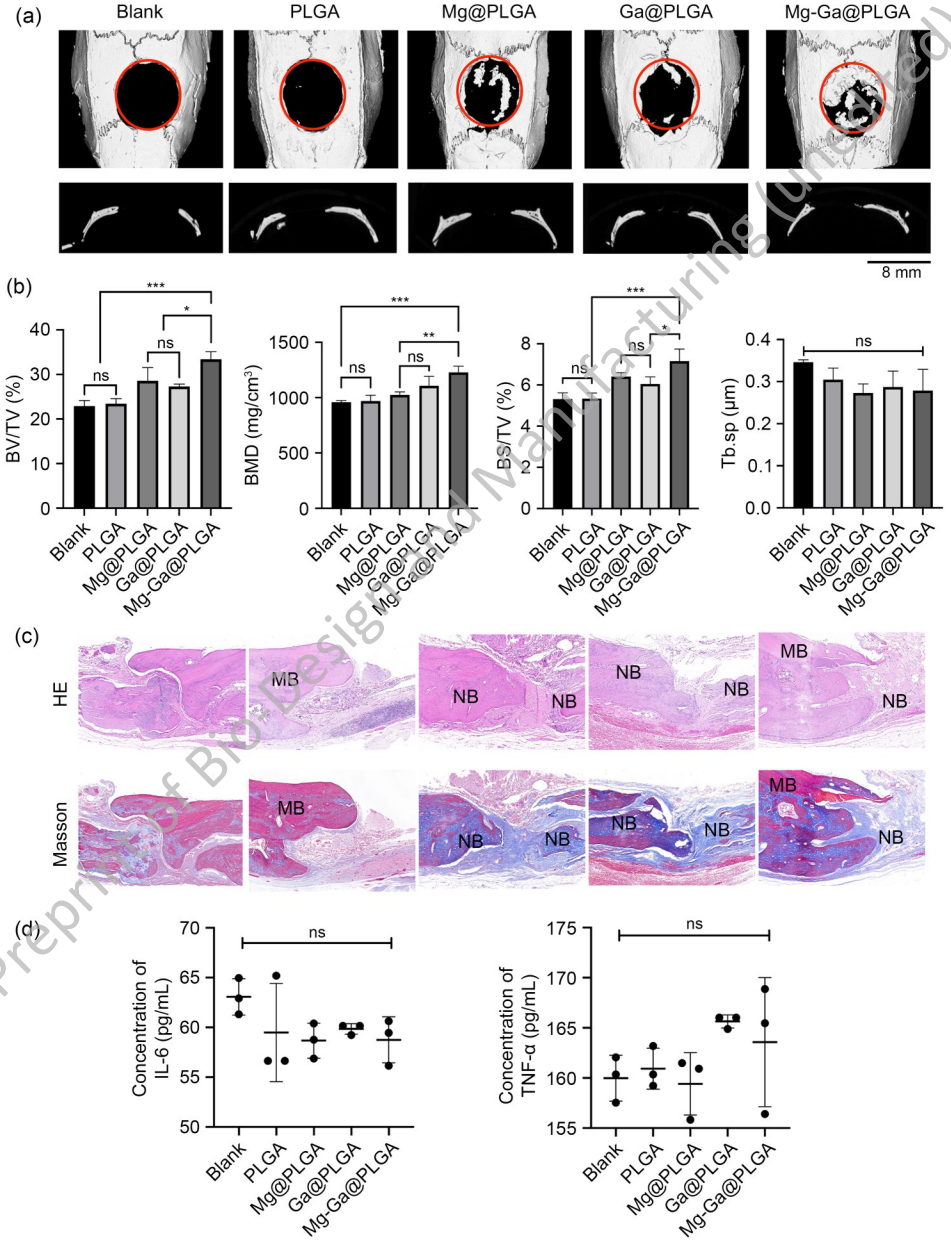

Fig. 7 Evaluation of bone formation at 12 weeks after implantation of PLGA, Mg@PLGA, Ga@PLGA, and Mg-Ga@PLGA microspheres. The control comprised the blank group. (a) Rat skulls reconstructed in three dimensions. (b) Quantification of the bone volume fraction in the defect site. (c) H&E and Masson trichrome staining at 12 weeks post-surgery. (d) Peripheral blood serology for the detection of inflammatory factors. (NB: new bone; and MB: mature bone) $^{*}p<0.05$, $^{**}p<0.01$, $^{***}p<0.001$

group exhibited the best repair ability according to micro-CT scans and bone parameters (Fig. 7b). For BV/TV, PLGA had the lowest bone volume fraction (23.45%). However, Mg@PLGA and Ga@PLGA induced better bone repair, at 28.57% and 27.32% respectively. Furthermore, Mg-Ga@PLGA showed the best bone repair ability, showing a bone volume fraction of 33.41% (p<0.01). BMD and BS/TV assessments showed similar results. Overall, the results for bone parameters were highly consistent with our micro-CT findings.

Next, H&E and Masson staining was used for histological analysis and to observe collagen growth, new bone tissue growth, and lymphocyte infiltration. Here, defects in the blank and PLGA groups mainly comprised fibrous tissue, with only a few (blue) collagen fibers. Moreover, we observed no prominent indications of new bone formation in these groups (Fig. 7c). In contrast, the Mg-Ga@PLGA groups had abundant collagen in bone defects, the stump was surrounded by new bone formation, and little fibrous connective tissue had infiltrated. In addition, H&E staining showed that all groups had low levels of lymphocyte infiltration, suggesting the absence of an inflammatory reaction [50] (Fig. 7c). Moreover, Masson and H&E staining also demonstrated that mature bone tissue grew in a lamellar pattern on a parallel bone plate structure, whereas new bone was mainly composed of collagen fibers undergoing mineralization; here we observed mainly round-like mineral deposits without a clear parallel hemipelagic bone structure. Peripheral blood serology also proved that there was no signifi7cant increase in inflammation in rat subjects (Fig. 7d).

Immunohistochemistry analyses detected the expression of Bmp2, collagen type I (COL I), osteocalcin (OCN), and osteopontin (OPN) (Fig. 8). At 12 weeks postsurgery, no significant OCN and COL I staining was seen in the control

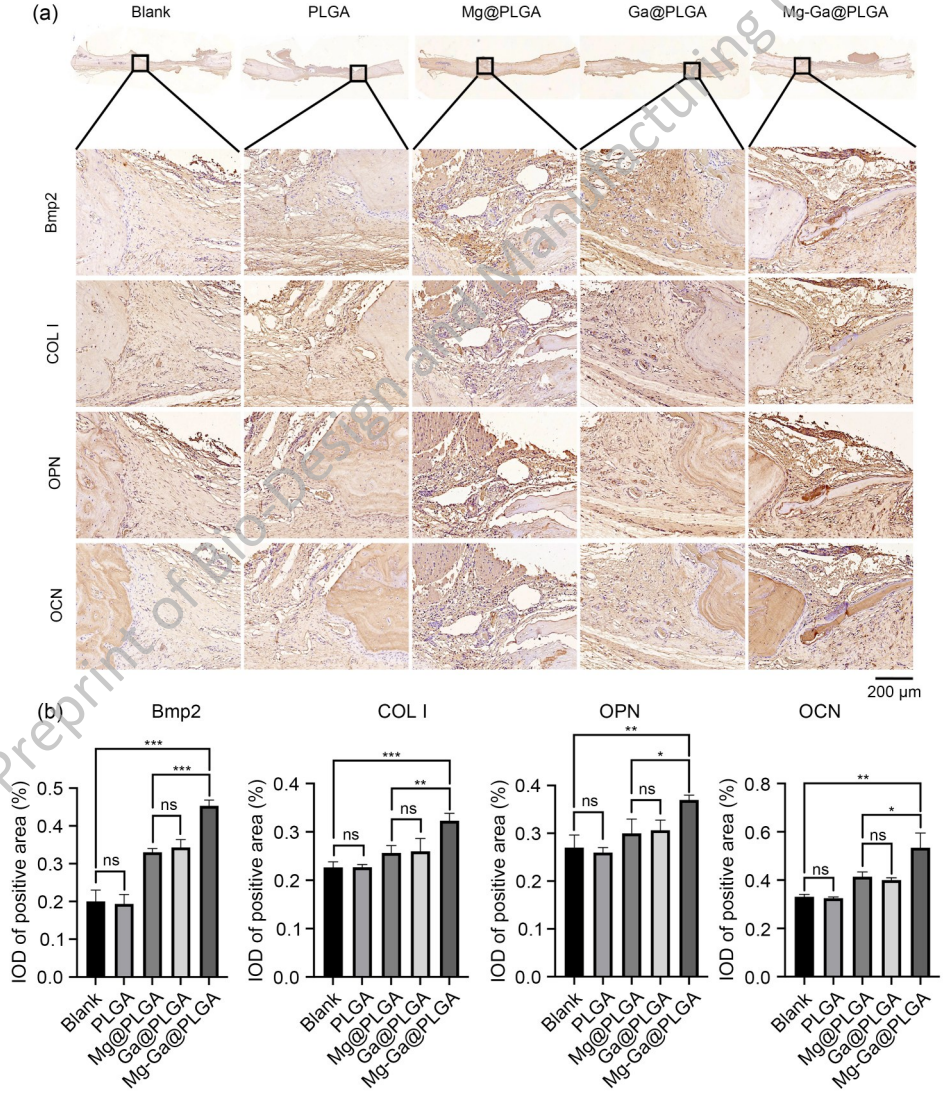

Fig. 8 Assessment of the osteogenesis effect of protein levels in vivo. (a) Immunohistochemical (IHC) analysis of Bmp2, COL I, OPN, and OCN to assess in vivo bone formation at 12 weeks post-surgery. (b) Quantification of the IHC results. $^{*}p$<0.05, $^{**}p$<0.01, $^{***}p$<0.001

group, whereas high levels were still observed in the Mg@PLGA, Ga@PLGA, and Mg-Ga@PLGA groups, with the highest levels found in the Mg-Ga@PLGA group. These findings were consistent with the micro-CT results reported above. Taken together, these results indicate that the coloading of Mg^{2+} and Ga^{3+} produced microspheres with excellent bone regenerative ability, and this effect may help to solve problems associated with bone defects. Moreover, the antibacterial ability of Mg-Ga@PLGA can prevent infection and associated tissue inflammation, and can thereby promote the repair of infected bone defects.

3.6 In vivo antibacterial activity

To verify the antibacterial effect of Mg-Ga@PLGA microspheres in animal models, we established infected bone defects with *S. aureus*, and collected the granulation tissue around the defects for further analysis. As shown in Fig. S4a, tissue samples derived from defects filled with PLGA microspheres exhibited significant bacterial clones. Clearly, a large number of bacterial colonies had formed in the Mg@PLGA group. However, the filling of Ga@PLGA and Mg-Ga@PLGA microspheres significantly reduced the survival proportion of *S. aureus* at the infection site compared to the PLGA and Mg@PLGA groups (Fig. S4b), and the inhibition of *S. aureus* was more pronounced in the Mg-Ga@PLGA group.

Our qRT-PCR analysis (Fig. S4c) showed that the Mg-Ga@PLGA microspheres exhibited the lowest expression of TNF-α and IL-6 ($p<0.0001$). Moreover, we also observed a significant decrease in the gene expression of TNF-α and IL-6, which were regarded as common infection indicators [46]. These findings suggest that Mg-Ga@PLGA microspheres may inhibit inflammatory responses caused by bacterial infection, and verify the antibacterial efficiency of Mg-Ga@PLGA microspheres in vivo. Interestingly, the microspheres coloaded with Mg^{2+} and Ga^{3+} showed a more significant antibacterial effect relative to the group with Ga^{3+} only, suggesting that the presence of Mg^{2+} enhanced the antibacterial effect of Ga^{3+}. Moreover, the expression of IL-6 was inhibited more significantly than that of TNF-α. Since the reason why this occurs remains unknown, the associated antimicrobial mechanism requires further exploration.

4 Conclusions

In this study, PLGA microspheres coloaded with Mg^{2+} and Ga^{3+} were prepared successfully and showed good biocompatibility and biosafety. We demonstrated that the Mg-Ga@PLGA microspheres have antibacterial effects, reducing the risk of infection and providing a microenvironment for bone defect repair. Meanwhile, Mg^{2+} and Ga^{3+} played a synergistic role in promoting osteogenic differentiation and inhibiting osteoclastic differentiation. Thus, Mg-Ga@PLGA microspheres have strong potential for use as a biomaterial to repair bone defects.

Acknowledgements This work was supported by grants from the National Natural Science Foundation of China (Nos. 31971106, BWS21L013, 21WS09002).

Author contributions Conceptualization, Jin Bai; Methodology, Jin Bai, Si Shen, Yan Liu, Tianqi Li; Investigation, Jin Bai, Si Shen, Yan Liu, Tianqi Li; Writing – Original Draft, Jin Bai; Writing – Review & Editing, All Authors;
Funding Acquisition, Xinxing Wang; Resources, Tianqi Li, Zirou Wang, Weili Liu, Lingling Pu; Supervision, Gang Chen, Xinxing Wang.

Declarations

Conflict of interest The authors declare that they have no conflicts of interest.

Ethical approval Ethical approvalAll animal experiments in this work were performed after obtaining permission from the institutional ethics board of Yi Shengyuan Gene Technology (Tianjin) Company.

References

1. Liu C, Qin W, Wang Y et al (2021) 3D printed gelatin/sodium alginate hydrogel scaffolds doped with nano-attapulgite for bone tissue repair. Int J Nanomedicine 16:8417–8432. https://doi.org/10.2147/ijn.S339500
2. Gillman CE, Jayasuriya AC (2021) FDA-approved bone grafts and bone graft substitute devices in bone regeneration. Mater Sci Eng C Mater Biol Appl 130:112466. https://doi.org/10.1016/j.msec.2021.112466
3. Stahl A, Yang YP (2021) Regenerative approaches for the treatment of large bone defects. Tissue Eng Part B Rev 27(6): 539–547. https://doi.org/10.1089/ten.TEB.2020.0281
4. Einhorn TA, Gerstenfeld LC (2015) Fracture healing: mechanisms and interventions. Nat Rev Rheumatol 11(1):45–54. https://doi.org/10.1038/nrrheum.2014.164
5. Zare S, Mohammadpour M, Izadi Z et al (2022) Nanofibrous hydrogel nanocomposite based on strontium-doped bioglass nanofibers for bone tissue engineering applications. Biology (Basel) 11(10):1472. https://doi.org/10.3390/biology11101472
6. Robbins S, Lauryssen C, Songer MN (2017) Use of Nanocrystalline hydroxyapatite with autologous BMA and local bone in the lumbar spine: a retrospective CT analysis of posterolateral fusion results. Clin Spine Surg 30(3):E192–E197. https://doi.org/10.1097/bsd.0000000000000091
7. Dasari A, Xue JY, Deb S (2022) Magnetic nanoparticles in bone tissue engineering. Nanomaterials (Basel) 12(5):757. https://doi.org/10.3390/nano12050757
8. Zong C, Van Holm W, Bronckaers A et al (2023) Biomimetic periodontal ligament transplantation activated by gold nanoparticles protects alveolar bone. Adv Healthc Mater 12(15):e2300328. https://doi.org/10.1002/adhm.202300328
9. Alonzo M, Alvarez Primo F, Anil Kumar S et al (2021) Bone tissue engineering techniques, advances and scaffolds for treatment of bone defects. Curr Opin Biomed Eng 17:100248.

https://doi.org/10.1016/j.cobme.2020.100248
10. Feng ZY, Su X, Wang T et al (2023) The role of microsphere structures in bottom-up bone tissue engineering. Pharmaceutics 15(2):321. https://doi.org/10.3390/pharmaceutics15020321
11. Vlachopoulos A, Karlioti G, Balla E et al (2022) Poly(Lactic Acid) -based microparticles for drug delivery applications: an overview of recent advances. Pharmaceutics 14(2):359. https://doi.org/10.3390/pharmaceutics14020359
12. Yu P, Yu FY, Xiang J et al (2022) Mechanistically scoping cell-free and cell-dependent artificial scaffolds in rebuilding skeletal and dental hard tissues. Adv Mater 34(46):e2107922. https://doi.org/10.1002/adma.202107922
13. Dong JJ, Wang B, Xiang BQ et al (2020) Research on the effect of TiO(2) nanotubes coated by gallium nitrate on Staphylococcus aureus-Escherichia coli biofilm formation. J Clin Lab Anal 34(9):e23417. https://doi.org/10.1002/jcla.23417
14. Caballero Aguilar LM, Duchi S, Onofrillo C et al (2021) Formation of alginate microspheres prepared by optimized microfluidics parameters for high encapsulation of bioactive molecules. J Colloid Interface Sci 587:240–251. https://doi.org/10.1016/j.jcis.2020.12.026
15. Li Q, Chang B, Dong H et al (2023) Functional microspheres for tissue regeneration. Bioact Mater 25:485–499. https://doi.org/10.1016/j.bioactmat.2022.07.025
16. Ciosek Ż, Kot K, Kosik-Bogacka D et al (2021) The effects of calcium, magnesium, phosphorus, fluoride, and lead on bone tissue. Biomolecules 11(4):506. https://doi.org/10.3390/biom11040506
17. Yoshizawa S, Chaya A, Verdelis K et al (2015) An in vivo model to assess magnesium alloys and their biological effect on human bone marrow stromal cells. Acta Biomater 28:234–239. https://doi.org/10.1016/j.actbio.2015.08.037
18. Buhrman G, Holzapfel G, Fetics S et al (2010) Allosteric modulation of Ras positions Q61 for a direct role in catalysis. Proc Natl Acad Sci USA 107(11):4931–4936. https://doi.org/10.1073/pnas.0912226107
19. Lin SH, Yin S, Shi JF et al (2022) Orchestration of energy metabolism and osteogenesis by Mg(2+) facilitates low-dose BMP-2-driven regeneration. Bioact Mater 18:116–127. https://doi.org/10.1016/j.bioactmat.2022.03.024
20. Zhang L, Yang CX, Li J et al (2014) High extracellular magnesium inhibits mineralized matrix deposition and modulates intracellular calcium signaling in human bone marrow-derived mesenchymal stem cells. Biochem Biophys Res Commun 450(4): 1390–1395. https://doi.org/10.1016/j.bbrc.2014.07.004
21. Chen YQ, Sheng WB, Lin JJ et al (2022) Magnesium oxide nanoparticle coordinated phosphate-functionalized chitosan injectable hydrogel for osteogenesis and angiogenesis in bone regeneration. ACS Appl Mater Interfaces 14(6):7592–7608. https://doi.org/10.1021/acsami.1c21260
22. de Baaij JHF, Hoenderop JGJ, Bindels RJM (2015) Magnesium in man: implications for health and disease. Physiol Rev 95(1): 1–46. https://doi.org/10.1152/physrev.00012.2014
23. Kurtuldu F, Mutlu N, Boccaccini AR et al (2022) Gallium containing bioactive materials: a review of anticancer, antibacterial, and osteogenic properties. Bioact Mater 17:125–146. https://doi.org/10.1016/j.bioactmat.2021.12.034
24. Goss CH, Kaneko Y, Khuu L et al (2018) Gallium disrupts bacterial iron metabolism and has therapeutic effects in mice and humans with lung infections. Sci Transl Med 10(460):eaat7520. https://doi.org/10.1126/scitranslmed.aat7520
25. Krakoff IH, Newman RA, Goldberg RS (1979) Clinical toxicologic and pharmacologic studies of gallium nitrate. Cancer 44(5):1722–1727. https://doi.org/10.1002/1097-0142(197911)44:5<1722::aid-cncr2820440528>3.0.co;2-c
26. Yu YL, Wu JJ, Lin CC et al (2023) Elimination of methicillin-resistant Staphylococcus aureus biofilms on titanium implants via photothermally-triggered nitric oxide and immunotherapy for enhanced osseointegration. Mil Med Res 10(1):21. https://doi.org/10.1186/s40779-023-00454-y
27. Li L, Chang H, Yong N et al (2021) Superior antibacterial activity of gallium based liquid metals due to Ga(3+) induced intracellular ROS generation. J Mater Chem B 9(1):85–93. https://doi.org/10.1039/d0tb00174k
28. Mao LX, Xia LG, Chang J et al (2017) The synergistic effects of Sr and Si bioactive ions on osteogenesis, osteoclastogenesis and angiogenesis for osteoporotic bone regeneration. Acta Biomater 61:217–232. https://doi.org/10.1016/j.actbio.2017.08.015
29. Zheng H, Huang ZD, Chen TX et al (2022) Gallium ions incorporated silk fibroin hydrogel with antibacterial efficacy for promoting healing of Pseudomonas aeruginosa-infected wound. Front Chem 10:1017548. https://doi.org/10.3389/fchem.2022.1017548
30. Tao BL, Zhao WK, Lin CC et al (2020) Surface modification of titanium implants by ZIF-8@Levo/LBL coating for inhibition of bacterial-associated infection and enhancement of in vivo osseointegration. Chem Eng J 390(C):124621. https://doi.org/10.1016/j.cej.2020.124621
31. Li K, Tian HC, Guo A et al (2022) Gallium (Ga)-strontium (Sr) layered double hydroxide composite coating on titanium substrates for enhanced osteogenic and antibacterial abilities. J Biomed Mater Res A 110(2):273–286. https://doi.org/10.1002/jbm.a.37284
32. Wei PF, Yuan ZY, Jing W et al (2018) Regenerating infected bone defects with osteocompatible microspheres possessing antibacterial activity. Biomater Sci 7(1):272–286. https://doi.org/10.1039/c8bm00903a
33. Kundu B, Rajkhowa R, Kundu SC et al (2013) Silk fibroin biomaterials for tissue regenerations. Adv Drug Deliv Rev 65(4): 457–470. https://doi.org/10.1016/j.addr.2012.09.043
34. Diban N, Gómez-Ruiz B, Lázaro-Díez M et al (2018) Factors affecting mass transport properties of poly(ε-caprolactone) membranes for tissue engineering bioreactors. Membranes (Basel) 8(3):51. https://doi.org/10.3390/membranes8030051
35. Pei YH, Wang JP, Khaliq NU et al (2023) Development of poly (lactide-co-glycolide) microparticles for sustained delivery of meloxicam. J Control Release 353:823–831. https://doi.org/10.1016/j.jconrel.2022.12.019
36. Saleh LS, Carles-Carner M, Bryant SJ (2018) The in vitro effects of macrophages on the osteogenic capabilities of MC3T3-E1 cells encapsulated in a biomimetic poly(ethylene glycol) hydrogel. Acta Biomater 71:37–48. https://doi.org/10.1016/j.actbio.2018.02.026
37. Jiang W, Hou FS, Gu Y et al (2022) Local bone metabolism balance regulation via double-adhesive hydrogel for fixing orthopedic implants. Bioact Mater 12:169–184. https://doi.org/10.1016/j.bioactmat.2021.10.017
38. Yang Y, Huang ZW, Li JY et al (2019) PLGA porous microspheres dry powders for codelivery of afatinib-loaded solid lipid nanoparticles and paclitaxel: novel therapy for EGFR tyrosine kinase inhibitors resistant nonsmall cell lung cancer. Adv Healthc Mater 8(23):e1900965.

https://doi.org/10.1002/adhm.201900965
39. Zhu JL, Liu YM, Chen C et al (2021) Cyasterone accelerates fracture healing by promoting MSCs migration and osteogenesis. J Orthop Translat 28:28–38. https://doi.org/10.1016/j.jot.2020.11.004
40. Xu JJ, Li Z, Tower RJ et al (2022) NGF-p75 signaling coordinates skeletal cell migration during bone repair. Sci Adv 8(11): eabl5716. https://doi.org/10.1126/sciadv.abl5716
41. Nakatsu Y, Nakagawa F, Higashi S et al (2018) Effect of acetaminophen on osteoblastic differentiation and migration of MC3T3-E1 cells. Pharmacol Rep 70(1):29–36. https://doi.org/10.1016/j.pharep.2017.07.006
42. Mariner PD, Johannesen E, Anseth KS (2012) Manipulation of miRNA activity accelerates osteogenic differentiation of hMSCs in engineered 3D scaffolds. J Tissue Eng Regen Med 6(4):314–324. https://doi.org/10.1002/term.435
43. Wang P, Liu X, Zhao L et al (2015) Bone tissue engineering via human induced pluripotent, umbilical cord and bone marrow mesenchymal stem cells in rat cranium. Acta Biomater 18:236–248. https://doi.org/10.1016/j.actbio.2015.02.011
44. Komori T (2017) Roles of runx2 in skeletal development. Adv Exp Med Biol 962:83–93. https://doi.org/10.1007/978-981-10-3233-2_6
45. Neill CJ, Harris S, Goldstone RJ et al (2020) Antibacterial activities of Ga(III) against E. coli are substantially impacted by Fe(III) uptake systems and multidrug resistance in combination with oxygen levels. ACS Infect Dis 6(11):2959–2969. https://doi.org/10.1021/acsinfecdis.0c00425
46. Wu JJ, Shen P, Qin X et al (2023) Self-supply of H2O2 and O2 by a composite nanogenerator for chemodynamic therapy/hypoxia improvement and rapid therapy of biofilm-infected wounds. Chem Eng J 459:141507. https://doi.org/10.1016/j.cej.2023.141507
47. Mosina M, Kovrlija I, Stipniece L et al (2022) Gallium containing calcium phosphates: potential antibacterial agents or fictitious truth. Acta Biomater 150:48–57. https://doi.org/10.1016/j.actbio.2022.07.063
48. Tao BL, Yi WW, Qin X et al (2023) Improvement of antibacterial, anti-inflammatory, and osteogenic properties of OGP loaded Co-MOF coating on titanium implants for advanced osseointegration. J Mater Sci Technol 146:131–144. https://doi.org/10.1016/j.jmst.2022.11.013
49. Lee DD, Galera-Laporta L, Bialecka-Fornal M et al (2019) Magnesium flux modulates ribosomes to increase bacterial survival. Cell 177(2):352–360. https://doi.org/10.1016/j.cell.2019.01.042
50. Ma SF, Feng XX, Liu FX et al (2021) The pro-inflammatory response of macrophages regulated by acid degradation products of poly(lactide-co-glycolide) nanoparticles. Eng Life Sci 21(10): 709–720. https://doi.org/10.1002/elsc.202100040